C. REDUCED AND SUPERREDUCED DIPLATINUM COMPLEXES

Reprinted with permission from Darnton, T. V; Hunter, B. M.; Hill, M.G.; Záliš, S.; Vlček Jr, A.; Gray, H.B. Reduced and Superreduced Diplatinum Complexes. *Journal of the American Chemical Society* **2016**, *138*, 5699. DOI: 10.1021/jacs.6b02559.

C.1. Abstract

A d^8-d^8 complex $[Pt_2(\mu\text{-}P_2O_5(BF_2)_4]^{4-}$ (abbreviated $Pt(pop\text{-}BF_2)^{4-}$) undergoes two $1e^-$ reductions at $E_{1/2}$ = -1.68 and E_p = -2.46 V (*vs*. Fc^+/Fc) producing reduced $Pt(pop\text{-}BF_2)^{5-}$ and superreduced $Pt(pop\text{-}BF_2)^{6-}$ species, respectively. The EPR spectrum of $Pt(pop\text{-}BF_2)^{5-}$ and UV-vis spectra of both the reduced and superreduced complexes, together with TD-DFT calculations, reveal successive filling of the 6pσ orbital accompanied by gradual strengthening of Pt–Pt bonding interactions and, because of 6pσ delocalization, of Pt–P bonds in the course of the two reductions. Mayer-Millikan Pt–Pt bond orders of 0.173, 0.268, and 0.340 were calculated for the parent, reduced, and superreduced complexes, respectively. The second (5–/6–) reduction is accompanied by a structural distortion that is experimentally manifested by electrochemical irreversibility. Both reduction steps proceed without changing either d^8 Pt electronic configuration, making the superreduced $Pt(pop\text{-}BF_2)^{6-}$ a very rare $6p^2$ σ-bonded binuclear complex. However, the Pt–Pt σ bonding interaction is limited by the relatively long bridging-ligand-imposed Pt–Pt distance accompanied by repulsive electronic congestion. $Pt(pop\text{-}BF_2)^{4-}$ is predicted to be a very strong photooxidant (potentials of +1.57 and +0.86 V are estimated for the singlet and triplet dσ*pσ excited states, respectively).

C.2. Introduction

The prototypal d^8-d^8 binuclear complex $Pt_2(P_2O_5H_2)_4^{4-}$ (abbreviated $Pt(pop)^{4-}$) and its perfluoroborated derivative $Pt_2(P_2O_5(BF_2)_2)_4^{4-}$ ($Pt(pop\text{-}BF_2)^{4-}$) have similar electronic structures and UV-vis absorption spectra, but profoundly different photophysics.[1,2] The

HOMO is a Pt–Pt σ-antibonding orbital (dσ*); interestingly, the LUMO is Pt–Pt bonding (pσ), albeit ~50% delocalized over the phosphorous ligands.[2] These two frontier orbitals are well separated from lower-lying occupied and higher unoccupied orbitals (Figure C.1). In $Pt(pop\text{-}BF_2)^{4-}$, pairs of bridging ligands are covalently connected by BF_2 groups, forming a rigid cage around the photo- and electroactive Pt–Pt unit that features outward facing fluorine atoms. This extra rigidity and shielding likely are responsible for the dramatically enhanced lifetime of the lowest $d\sigma^* \rightarrow p\sigma$ singlet excited state (1.6 ns *vs*. ca. 3 ps for $Pt(pop)^{4-}$).[1,3] Electron excitation into the pσ orbital strengthens the Pt–Pt interaction, as evidenced by 0.18 Å bond shortening (calc'd for $Pt(pop\text{-}BF_2)$;[2] 0.21-0.31 Å determined[4-7] by X-ray and optical techniques for Pt(pop)) and a 38-45 cm^{-1} increase of the Pt–Pt stretching frequency in both Pt(pop) and $Pt(pop\text{-}BF_2)$.[3,6-9] In analogy to optical excitation, reduction is expected to fill the pσ orbital, forming a weak Pt–Pt bond in $Pt(pop\text{-}BF_2)^{5-}$. Although reversible electrochemical reduction of $Pt(pop)^{4-}$ has not been reported,[10] $Pt(pop)^{5-}$ with a 34 μs lifetime was generated by pulse radiolysis in aqueous solution.[11] What is more, transient generation of a reduced species was indicated by observation of electrochemiluminescence at a platinum electrode in MeCN upon high-frequency potential switching.[12,13] As reducible –O–H···O– hydrogens are absent in $Pt(pop\text{-}BF_2)^{4-}$, we thought it likely that the complex could be reduced reversibly, and we have observed a two-step sequential reduction of $Pt(pop\text{-}BF_2)^{4-}$. The electronic structures of the two reduced forms have been investigated by DFT as well as spectroelectrochemical methods.

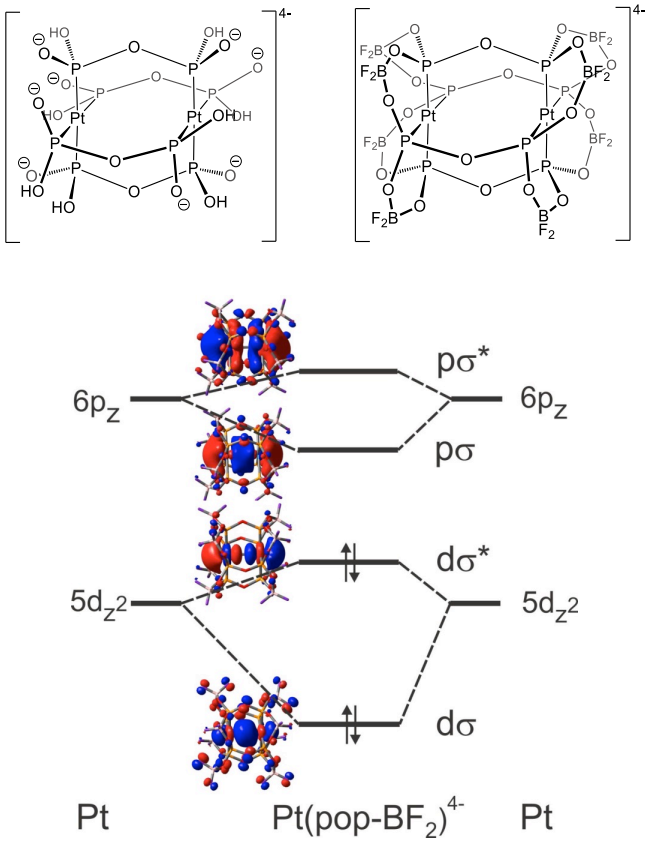

Figure C.1. Structural representations of $Pt(pop)^{4-}$ and $Pt(pop\text{-}BF2)^{4-}$ along with a qualitative σ-MO scheme.

C.3. Results

$Pt(pop\text{-}BF_2)^{4-}$ in MeCN at 273 K undergoes one-electron reductions at $E_{1/2}$ = -1.68 and E_p = -2.46 V *vs*. Fc^+/Fc (Figure C.2.2). The first wave is chemically reversible and electrochemically quasireversible at a scan rate of 50 mV/s (ΔE_p = 155 mV; compared with ~100 mV obtained for Fc^+/Fc under virtually identical conditions). The second wave is electrochemically irreversible and chemically reversible, indicating formation of a superreduced complex $Pt(pop\text{-}BF_2)^{6-}$, stable at least at 273 K. At room temperature, the peak-current ratio of the second wave is less than unity and two small shoulders appear at its positive site, attributable to decomposition products. Scanning over the anodic region reveals a 2-electron chemically irreversible oxidation at +0.94 V (*vs*. Fc^+/Fc).

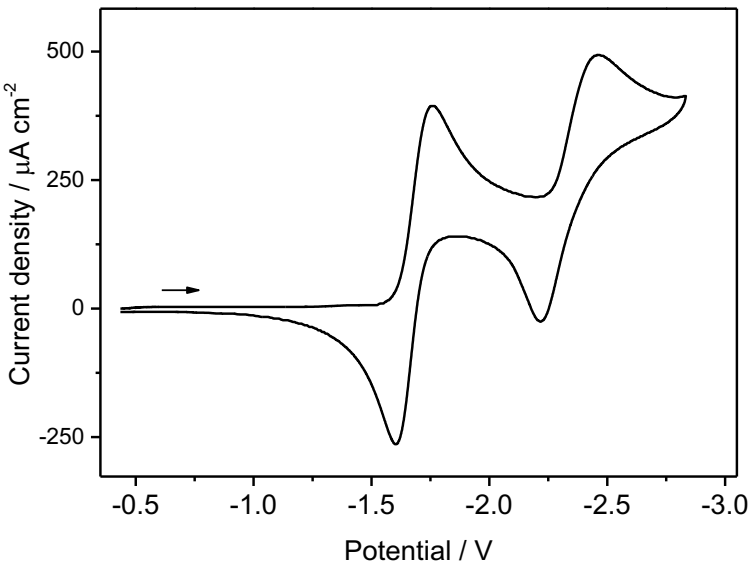

Figure C.2. Cyclic voltammogram of $Pt(pop\text{-}BF_2)^{4-}$ in MeCN containing 0.1 M Bu_4NPF_6 at 273 K. Potentials vs. Fc+/Fc. Scan rate 50 mV/s.

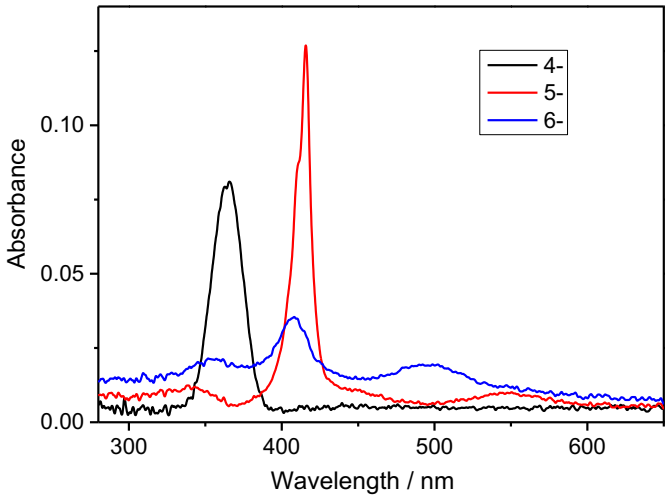

Figure C.3. UV-vis absorption spectra of $Pt(pop\text{-}BF_2)^{4-}$ (black) and in-situ spectroelectrochemically produced $Pt(pop\text{-}BF_2)^{5-}$ (red) and $Pt(pop\text{-}BF_2)^{6-}$ (blue, contains ca. 20% of $Pt(pop\text{-}BF_2)^{5-}$). Conditions: glassy carbon working electrode, MeCN, 0.1 M Bu_4NPF_6, 273 K. Binomial smoothing applied.

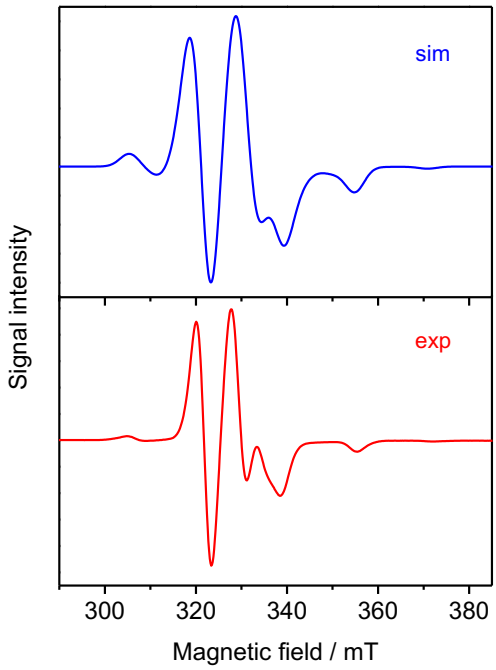

Figure C.4. Experimental (bottom) and simulated (top) EPR spectra of $Pt(pop\text{-}BF_2)^{5-}$ obtained after $Pt(pop\text{-}BF_2)^{4-}$ reduction with Na/Hg in MeCN at room temperature. Simulated parameters: g_1 = 1.98, g_2 = 2.03, g_3 = 2.04; A(Pt) = 550, 550, 900 MHz; A(Pt') = 350, 500, 900 MHz.

UV-vis spectroelectrochemistry in MeCN at 273 K carried out at the potential of the first reduction wave shows a decrease in intensity of the 365-nm band of $Pt(pop\text{-}BF_2)^{4-}$ accompanied by a rise of a sharp band at 416 nm with shoulders at ca. 411 and ~450 nm, and broad weak bands at ~550 and 338 nm, all attributable to $Pt(pop\text{-}BF_2)^{5-}$ (C.3). The parent complex is nearly quantitatively recovered upon anodically switching the potential. Further reduction at more negative potentials yields a spectrum with three distinct features (356, 408 and 496 nm; Figure C.3). Spectra measured in the course of the second reduction show an isosbestic point, indicating conversion to the superreduced species $Pt(pop\text{-}BF_2)^{6-}$. Reoxidation at more positive potentials initially recovers $Pt(pop\text{-}BF_2)^{5-}$ at 273 K, whereas an unidentified species strongly absorbing at 350 nm is formed at room temperature. Experimental spectra of both the reduced and superreduced species match those calculated by TD-DFT, supporting their assignments as $Pt(pop\text{-}BF_2)^{5-}$ and $Pt(pop\text{-}BF_2)^{6-}$, respectively.

The reduced species $Pt(pop\text{-}BF_2)^{5-}$ also was characterized by EPR, after reduction with Na/Hg and freezing to 77 K. Both experimental and simulated spectra are shown in Figure B.4. The EPR spectrum is characteristic of a spin-doublet state with an axial spin distribution ($g_2 \cong g_3 \neq g_1$). Hyperfine splitting constants due to the two ^{195}Pt nuclei are similar, indicating a nearly symmetrical spin density distribution. The g values are similar to those determined for Pt(II) complexes with radical-anion ligands.[14,15] In contrast, "platinum blue" species, where the unpaired electron is delocalized over four Pt atoms in a molecular orbital with predominantly 5d-character, also exhibit axial EPR spectra but with much larger g values as well as pronounced anisotropy.[16,17] Still larger g-values have been reported for Pt(I) d^9 sites.[18] The EPR data for $Pt(pop\text{-}BF_2)^{5-}$ suggest that the unpaired electron is delocalized over the two Pt atoms as well as the ligands in a molecular orbital of 6p-character. Our interpretation is supported by DFT spin-density calculations (Figure C.5), which accurately reproduce the g-values.

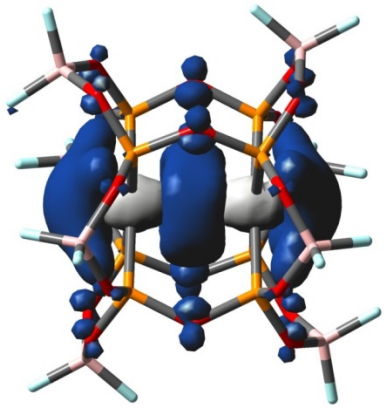

Figure C.5. DFT(PBE0/PCM-MeCN) calculated spin-density distribution in $Pt(pop\text{-}BF_2)^{5-}$ in MeCN solution.

C.3.1. Molecular and electronic structures: DFT calculations

DFT optimizations of the reduced and superreduced species in MeCN were performed without symmetry constraints. Calculations started from several different initial structures, including asymmetric ones, to ensure that the absolute energy minimum was found. Structural optimization shows successive Pt-Pt and Pt-P bond shortening upon each one-electron reduction (Table C-1). The P_4Pt units, which are almost planar in $Pt(pop\text{-}BF_2)^{4-}$, bend slightly outwards upon the first reduction. The two platinum atoms remain approximately equivalent, as evidenced by nearly identical Pt(1)–P and Pt(2)–P distances. The inclusion of five Me_4N^+ cations in the calculation did not change the symmetrical molecular structure of $Pt(pop\text{-}BF_2)^{5-}$, although the cations adopted an asymmetric distribution around the 5– anion.

Two stable structures were calculated for superreduced $Pt(pop\text{-}BF_2)^{6-}$. The slightly asymmetric conformation (denoted **6**) is the more stable one with small angular distortions around the Pt atoms (Table C-1). The other calculated conformation (**6'**) is nearly symmetrical, much like the 5– species, with the Pt atoms displaced inwards with respect to the surrounding P_4 planes. The calculated free energy of **6'** is 0.096 eV higher than that of **6** and the Pt–Pt and Pt–P bonds are shorter relative to $Pt(pop\text{-}BF_2)^{5-}$ in both conformations. Structural optimization in the presence of six Me_4N^+ cations yields a structure similar to **6**, with an asymmetrical distribution of cations.

Table C-1: Selected bond lengths (Å) of $Pt(pop\text{-}BF_2)^{n-}$ (n = 4, 5, 6) calculated by DFT(PBE0/PCM-MeCN).

n =	4	5	Δ(5 – 4)	6	Δ(6 – 5)	6'	Δ(6' – 5)
Pt-Pt	2.887	2.803	-0.084	2.739	-0.058	2.745	-0.058
Pt-P (average)	2.301	2.278	-0.025	2.255	-0.023	2.255	-0.023
P-O(-P) (average)	1.625	1.634	0.009	1.643	0.010	1.644	0.010
P-Pt-P (average)	178.8[a]	177.1[a]	-1.7	166.8[a] -175.7[b]	-10.3 7.2	176.0[a]	-1.1

[a] The P→Pt vectors point inwards to the Pt–Pt unit. [b] The P→Pt vectors point outwards from the Pt–Pt unit. The Pt–P directions are reversed at the other PtP_4 unit.

The two reduction steps correspond to successive filling of the pσ orbital (Figure C.1), whose calculated Pt character increases from 43% in the parent complex to about 59% in both the 5– and 6– species. Accordingly, the calculated spin density in $Pt(pop\text{-}BF_2)^{5-}$ is nearly symmetrically distributed between and around the two Pt atoms (Figure C.5). The strong narrow band in the $Pt(pop\text{-}BF_2)^{5-}$ UV-vis absorption spectrum is due to a transition of predominantly βHOMO→βLUMO (dσ*→pσ) character (Table C-2, Figure C.6); it is red-shifted relative to the corresponding band of the parent complex (416 vs. 365 nm[1]), but of comparable integrated intensity (Figure C.3). The high-energy shoulder is attributable to vibronic structure: corresponding peak wavenumbers of 24050 and 24380 cm^{-1}, separated by 330 cm^{-1}, were obtained by Gaussian decomposition. (The absorption band can be decomposed into four Gaussians with an average separation of 270 cm^{-1}.) Several mixed δ(POP)/ν(PtPt) vibrations are expected[3] to occur in this frequency range. The lowest absorption band (550 nm) of $Pt(pop\text{-}BF_2)^{5-}$ has no counterpart in the $Pt(pop\text{-}BF_2)^{4-}$ spectrum. The transition in question predominantly involves excitation from a pσ orbital (αHOMO) to a ligand-localized molecular orbital that also contains a dσ* admixture (αLUMO). This

transition gains intensity from the 23% contribution of βHOMO→βLUMO (dσ*→pσ) excitation (Table C-2).

Table C-2: TD-DFT (PBE0/PCM-MeCN) calculated lowest doublet excitation energies for $Pt(pop\text{-}BF_2)^{5-}$. The MOs (spin-orbitals) involved in the lowest excitations are depicted in Figure 6; αLUMO+6 and αLUMO+7 are mostly localized on pop-BF_2.

State	Main contributing excitations (%)	Transition energy eV (nm)	Oscillator strength	Exptl. nm
b^2A	99 (αHOMO → αLUMO+1)	2.32 (533)	0.0[a]	
c^2A	70 (αHOMO → αLUMO) 23 (βHOMO → βLUMO)	2.43 (509)	0.036	~550
d^2A	99 (αHOMO → αLUMO+2)	2.46 (505)	0.0[a]	~450
e^2A	74 (βHOMO → βLUMO) 25 (αHOMO → αLUMO)	3.02 (411)	0.285	416
f^2A	90 (αHOMO → αLUMO+6)	3.82 (325)	0.009	338
g^2A	99 (αHOMO → αLUMO+7)	3.82 (325)	0.015	

[a] Oscillator strengths become nonzero (~2×10^{-4}) when spin-orbit coupling is approximately included.

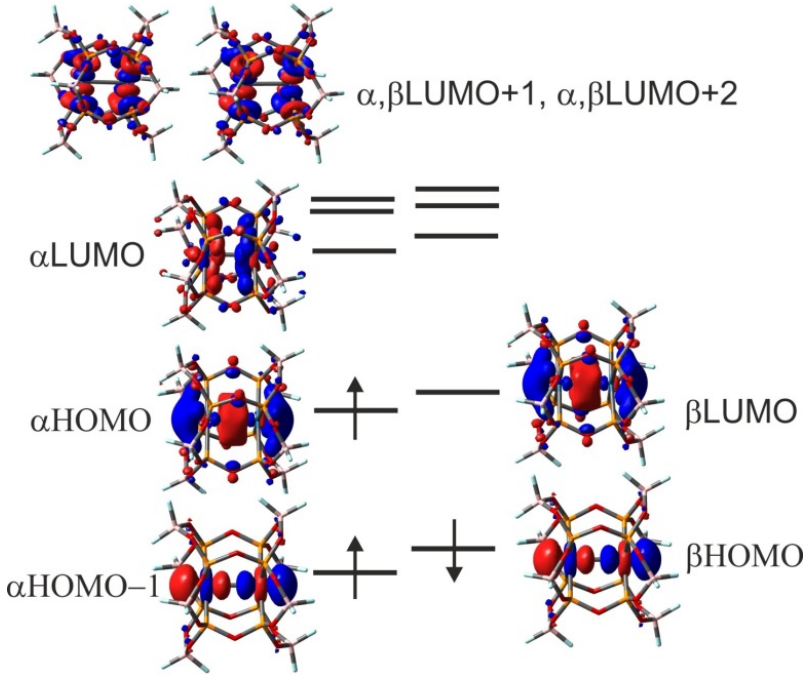

Figure C.6. Frontier molecular orbitals (spin-orbitals) involved in the lowest electronic transitions of $Pt(pop\text{-}BF_2)^{5-}$.

The doubly occupied pσ HOMO in the superreduced species **6** is polarized toward one of the Pt atoms (Figure C.7), making the electron distribution slightly asymmetric. Each Pt atom in **6** formally keeps its $5d^8$ electron configuration, while the two Pt atoms are connected by a 2-electron σ-bond arising from $6p_z$–$6p_z$ orbital overlap. With a $(d\sigma^*)^2(p\sigma)^2$ configuration, spectroscopically relevant electronic transitions are unrelated to those of the parent complex. These transitions, which originate from the pσ HOMO, are directed into higher unoccupied orbitals of mixed metal/ligand character (Table C-3). The lowest broad band due to the HOMO→LUMO transition involves a small electron-density shift between the Pt atoms; the transition weakens the Pt–Pt bond both because of HOMO(pσ) depopulation and the partial pσ* character of the LUMO. The absorption spectrum calculated for the more symmetrical configuration **6'** shows only one principal band. It is very different from both the experimental spectrum and the spectrum calculated for **6**.

Table C-3: TD-DFT (PBE0/PCM-MeCN) calculated lowest singlet excitation energies (eV) for $Pt(pop\text{-}BF_2)^{6-}$/conformation **6**. The relevant MOs are depicted in Figure B.7.

State	Main contributing excitations (%)	Transition energy eV (nm)	Oscillator strength	Exptl. eV (nm)
b^1A	90 (HOMO → LUMO)	2.53 (490)	0.184	496
c^1A	80 (HOMO → LUMO+1) 10 (HOMO → LUMO+4)	3.07 (404)	0.075	408
d^1A	87 (HOMO → LUMO+4) 12 (HOMO → LUMO+1)	3.53 (350)	0.081	356
e^1A	92 (HOMO → LUMO+6)	4.00 (310)	0.016	
f^lA	70 (HOMO → LUMO+7)	4.08 (304)	0.013	

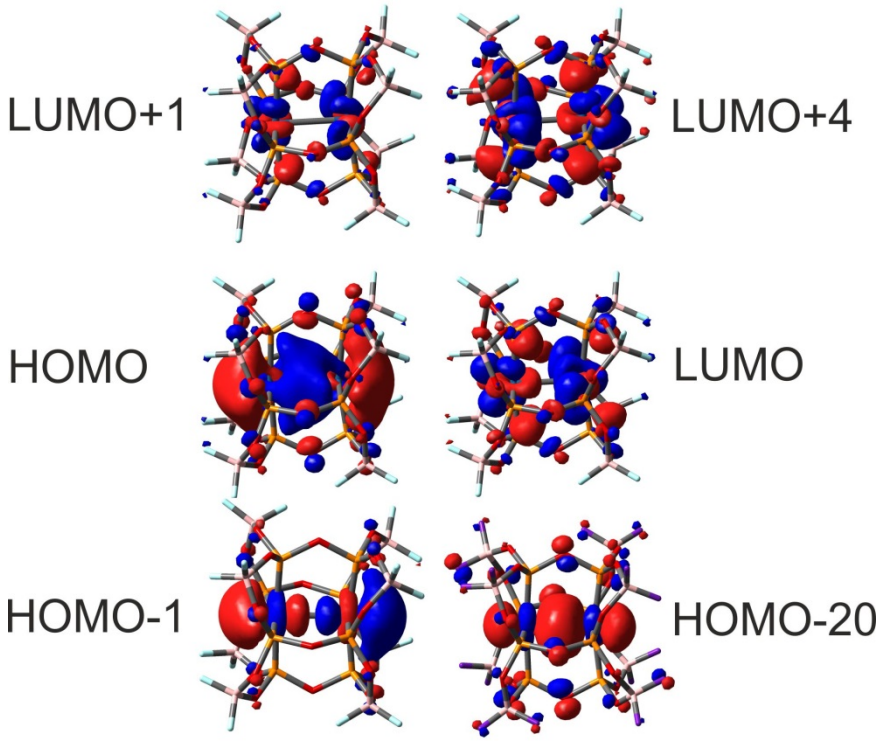

Figure C.7. Frontier molecular orbitals involved in the lowest electronic transitions of $Pt(pop\text{-}BF_2)^{6-}$/conformer **6**. HOMO is the 6pσ orbital; HOMO-1 and HOMO-20 are the 5dσ* and 5dσ orbitals, respectively.

C.4. Discussion

Perfluoroboration strongly stabilizes reduced forms of $Pt(pop)^{4-}$. The reduced $Pt(pop\text{-}BF_2)^{5-}$ and superreduced $Pt(pop\text{-}BF_2)^{6-}$ are stable in MeCN solution at least on the order of minutes, compared with μs-ms times[11,12] in the case of $Pt(pop)^{5-}$ (and it is not likely that $Pt(pop)^{6-}$ can be isolated[19]). The enhanced stability of the reduced and superreduced forms is attributable to the lack of reducible hydrogen atoms in the covalently linked inorganic cage around the Pt–Pt unit. The large potential difference (~0.7 V) between the first and second reductions indicates that disproportionation of $Pt(pop\text{-}BF_2)^{5-}$ is disfavored.

The first reduction of $Pt(pop\text{-}BF_2)^{4-}$ occurs at -1.68 V (vs Fc^+/Fc), as compared with ca. -1.8 V for Pt(pop). (The Pt(pop) value was estimated[20] from excited-state reductive

quenching kinetics in MeOH. No electrochemical reduction wave was reported.) This redox-potential difference is attributable to the electron-withdrawing effect of BF_2, transmitted to the Pt–Pt unit by pσ delocalization over the P donor atoms (Figures B.1, B.6, B.7). It follows that electronically excited $Pt(pop\text{-}BF_2)^{4-}$ is a very strong oxidant: potentials of +1.57 and +0.86 V (vs Fc^+/Fc) can be estimated for $*^1Pt(pop\text{-}BF_2)^{4-/5-}$ and $*^3Pt(pop\text{-}BF_2)^{4-/5-}$ redox couples, respectively (using spectroscopically determined excited-state energies[3]). Owing to the stability of the reduced species and the shielding effect of the eight BF_2 groups, reductive quenching of excited $Pt(pop\text{-}BF_2)^{4-}$ should be reversible and occur with a high cage-escape yield (80% was reported[20] for quenching of $*^3Pt(pop)$ by dimethylaniline). $Pt(pop\text{-}BF_2)^{4-}$ thus emerges as a promising photooxidant that could be employed to drive steps in organic reactions.

The reduced species $Pt(pop\text{-}BF_2)^{5-}$ can be generated by electrochemical or chemical reduction and also by irradiating the parent complex in the presence of an irreversible reductive quencher.[21] It could reduce substrates in reactions involving both outer and inner sphere activation. However, the radical-like reactivity typical for $*^3Pt(pop)$[22-24] is not expected for the reduced species, since the outward-oriented dσ* orbital is doubly occupied, unlike the excited state. The superreduced $Pt(pop\text{-}BF_2)^{6-}$ can only be produced electrochemically or by using very strong chemical reductants. In a preliminary experiment, we found $Pt(pop\text{-}BF_2)^{6-}$ to be much more reactive toward CH_2Cl_2 than $Pt(pop\text{-}BF_2)^{5-}$. Rates of outer-sphere electron transfer reactions of $Pt(pop\text{-}BF_2)^{6-}$ will be limited by large reorganization energies, as indicated by the electrochemical irreversibility of the 5-/6- CV wave at the 50 mV/s scan rate (Figure B.2). The relatively slow second reduction step correlates with increasing structural reorganization, as revealed by DFT (Table B-1).

Spectroscopic changes recorded in the course of the reduction together with DFT calculations point to successive filling of the pσ molecular orbital: the strong, sharp $d\sigma^* \rightarrow p\sigma$ band is the lowest-energy feature in the spectrum of the parent complex. It also is present in the reduced (5–) species with a $(d\sigma^*)^2(p\sigma)^1$ configuration but preceded in energy by a weaker band attributable to pσ excitation (Table B-2). The UV-vis spectral pattern changes

completely in the superreduced complex, as the pσ orbital becomes fully occupied. The dσ*→pσ transition vanishes and the spectrum exhibits a series of transitions from the pσ HOMO to higher unoccupied orbitals (Table B-3).

Successive filling of the pσ orbital formally generates a Pt–Pt σ bond without changing the Pt $5d^8$ electronic configuration, making $Pt(pop\text{-}BF_2)^{6-}$ a very rare $6p^2$ σ-bonded binuclear complex. The DFT-calculated Mayer-Mulliken bond orders[25] show strengthening of the Pt–Pt bonding interaction upon reduction (Table B-4), whereby the bond order increases about two-fold on going from the 4– parent (0.17) to the 6– superreduced complex (0.34). While significant, the Pt–Pt bonding in $Pt(pop\text{-}BF_2)^{6-}$ is far from a full σ-bond. The Pt–Pt bonding interaction is limited by several structural and electronic factors: the rigid pop-BF_2 ligand cage does not allow the metal-metal distance to shorten very much, disfavoring effective orbital overlap; the $(5d\sigma)^2(5d\sigma^*)^2(6p\sigma)^2$ configuration places six σ electrons in spatial proximity with one another, producing repulsive electronic congestion along the Pt–Pt axis; and the pσ molecular orbital is only 59% $6p_z$ in character, being delocalized over the Pt-P bonds (Figures B.1, B.6, B.7). Accordingly, Pt–P bond orders also gradually increase upon reduction (Table B-4). The EPR spectrum of $Pt(pop\text{-}BF_2)^{5-}$ confirms the delocalized nature of the singly occupied 6pσ molecular orbital, showing axial spin density distribution.

Table C-4: DFT-calculated Mayer-Mulliken bond orders for $Pt(pop\text{-}BF_2)^{n-}$ complexes. Atom P5 is in alignment with atom P1, etc.

bond \ n	4	5	6/conf. **6**
Pt - Pt	0.173	0.268	0.340
Pt – P1	1.119	1.181	1.175
Pt – P2	1.122	1.173	1.309
Pt – P3	1.122	1.173	1.167
Pt – P4	1.119	1.182	1.312
Pt – P5	1.119	1.183	1.320
Pt – P6	1.121	1.174	1.175
Pt – P7	1.121	1.175	1.328
Pt – P8	1.119	1.183	1.168

The Pt–Pt distance was calculated to shorten by 0.08 and 0.06 Å upon the first and second reductions, respectively, while the calculated Pt–Pt stretching frequency ν(Pt–Pt) increases from 128 cm^{-1} in the parent complex to 146 (5–) and 170 cm^{-1} (6–). The reduced species essentially keeps the high symmetry of the parent complex, which is manifested both by the calculation and the EPR spectrum. The most stable conformer of $Pt(pop\text{-}BF_2)^{6-}$ shows a small asymmetry, both between the two Pt centers and within each PtP_4 unit, where one pair of *trans* Pt-P bonds is shorter than the other. The HOMO also is distributed slightly asymmetrically, perhaps due to the "frustrated" pσ interaction mentioned above. Nevertheless, the calculated natural charges at the two Pt atoms differ by only 0.035 e^-, in accordance with the $(5d\sigma)^2(5d\sigma^*)^2(6p\sigma)^2$ configuration. This behavior contrasts with that of doubly-reduced $5d^8$-$5d^8$ $Ir_2(dimen)_4^{2+}$ (dimen = 1,8-diisocyano-*p*-menthane) that adopts a d^8-

d^{10} (Ir^{II}-Ir^{0}) mixed-valence configuration. In this case, one iridium center maintains a square planar local geometry, while the other distorts toward tetrahedral.[26] Such a distortion avoids the congested $(5d\sigma)^2(5d\sigma^*)^2(6p\sigma)^2$ electronic structure and its stabilizing effect is manifested by the much smaller difference between the first and second reduction potentials of $Ir_2(dimen)_4^{2+}$ (0.19 V),[26] as compared with Pt(pop-BF2) (~0.7 V). Such a distortion toward a mixed-valence structure is possible in the $Ir_2(dimen)_4^{2+}$ case because of the structural flexibility of the dimen bridge,[27] whereas the rigid pop-BF_2 ligand cage of $Pt(pop\text{-}BF_2)^{6-}$ enforces a nearly symmetrical structure, producing the unusual partial 6pσ metal-metal bond. We plan to map the reactivity patterns of this powerful $(6p)^2$ σ-bond reductant.

C.5. Experimental

Materials and procedures. $[Bu_4N]_4[Pt_2(P_2O_5(BF_2)_2)_4]$ was prepared as described previously.[1,21] All measurements were performed under an argon atmosphere in dry, degassed acetonitrile (HPLC grade, Fisher) that was passed through a solvent purification column. Bu_4NPF_6 (Fluka) was used as received. Electrolyte solutions were prepared and stored over activated alumina and 4-Å molecular sieves.

All electrochemical experiments were performed with a CH Instruments Model 650A electrochemical analyzer. Cyclic voltammetry (CV) at ambient temperature was measured in a three-electrode configuration consisting of a highly polished glassy-carbon-disk working electrode (A = 0.07 cm^2), a Pt wire auxiliary electrode, and a 1.0 M KCl AgCl/Ag reference electrode, separated by a modified Luggin capillary. Low temperature CV was carried out using a nonisothermal cell configuration, in which the reference electrode was held at ambient temperature, separated from the working compartment by a long glass tube filled with electrolyte, and connected by a Luggin capillary. The temperature was monitored by a thermocouple placed in the working compartment. Potentials in the figures are reported vs. aqueous AgCl/Ag, not corrected for the junction potential. The ferrocenium/ferrocene couple has $E^{0'}$ = 0.434 V, measured at identical experimental conditions. All potentials in the text are reported vs. Fc^+/Fc.

Thin-layer spectroelectrochemistry was carried out in a specular-reflectance mode using a modified IR cell. An Ocean Optics UV-vis light source (DH-2000) and spectrometer (USB2000) were connected to the Y-arms of a bifurcated fiber-optic cable; the end of the cable was connected through a lens housing containing a semi-spherical collimating lens to the front-face window of the spectroelectrochemical cell at a 90 degree angle. A drop of mineral oil between the fiber optic and front-face quartz window of the cell ensures refractive-index matching. Spectra were not corrected for front-face reflection. The error in intensity at an absorbance of 0.5 is less than 1%. The glassy-carbon working electrode of the spectroelectrochemical cell was attached with silver epoxy to a brass cooling tube, connected to a circulating variable-temperature bath.

EPR spectra were recorded on a Bruker EMS spectrometer at 9.39 GHz. Samples at ~10 mM concentration were prepared by reduction with Na/Hg in dry acetonitrile under an N_2 atmosphere and frozen with liquid nitrogen prior to the measurements. Spectral simulations were performed with MATLAB using the EasySpin MATLAB toolbox (version 4.5.5). Simulation parameters obtained: g = [2.04, 2.03, 1.98]; HStrain = [180, 120, 100] MHz; A_{Pt1} = [550, 550, 900] MHz; A_{Pt2} = [350, 500, 900] MHz.

DFT Calculations. Electronic structures of $Pt(pop\text{-}BF_2)^{n-}$ (n = 4, 5, 6) complexes were calculated by density functional theory (DFT) methods using Gaussian 09[28] (G09) and ADF 2014.06[29] program packages. All calculations employed the hybrid Perdew, Burke and Ernzerhof[30,31] (PBE0) exchange and correlation functional. The following basis sets were used within G09: 6-311g(3d) polarized triple-ζ basis sets[32] for P and O; 6-31g(d) double-ζ for remaining first row atoms, and quasi-relativistic small-core effective core pseudopotentials and the corresponding optimized set of basis functions for Pt.[33,34] Mayer-Mulliken bond orders and natural charges were calculated by NBO 6.0 program.[35]

The solvent was included using the polarizable calculation model (PCM).[36] Geometry optimizations, which were performed without any symmetry constraints, included the PCM solvent correction.[36] They were followed by vibrational analysis: no imaginary frequencies

were found for energy minima. Open-shell systems were treated by the unrestricted Kohn–Sham (UKS) procedure. For comparison of spectra in different redox states, Me_4N^+ counter-ions corresponding to the negative charge of the complex anion were added. ADF calculations employed Slater-type orbital (STO) basis sets of triple-ζ quality with two polarization functions for the Pt atom, triple-ζ with polarization functions for O, P, and H atoms, and double-ζ with one polarization function for the remaining atoms. The basis set was represented by a frozen core approximation (1s for B, N, O, 1s-2p for P and 1s-4d for Pt were kept frozen). The scalar relativistic (SR) zero order regular approximation (ZORA) was used. Solvent effect corrections were calculated using the COSMO model.[37] The *g* tensor was obtained from a spin-nonpolarized wave function after incorporating spin-orbit (SO) coupling.[38] EPR parameters were calculated by single point procedures at optimized structures.

C.6. References and Notes

(1) Durrell, A. C.; Keller, G. E.; Lam, Y.-C.; Sýkora, J.; Vlček, A., Jr.; Gray, H. B. *J. Am. Chem. Soc.* **2012**, *134*, 14201−14207.

(2) Záliš, S.; Lam, Y. C.; Gray, H. B.; Vlček, A., Jr. *Inorg. Chem.* **2015**, *54*, 3491−3500.

(3) Hofbeck, T.; Lam, Y. C.; Kalbáč, M.; Záliš, S.; Vlček, A.; Yersin, H. *Inorg. Chem., submitted* **2016**.

(4) van der Veen, R. M.; Milne, C. J.; El Nahhas, A.; Lima, F. A.; Pham, V.-T.; Best, J.; Weinstein, J. A.; Borca, C. N.; Abela, R.; Bressler, C.; Chergui, M. *Angew. Chem. Int. Ed.* **2009**, *48*, 2711 –2714.

(5) Christensen, M.; Haldrup, K.; Bechgaard, K.; Feidenhans'l, R.; Kong, Q.; Cammarata, M.; Lo Russo, M.; Wulff, M.; Harrit, N.; M.M., N. *J. Am. Chem. Soc.* **2009**, *131*, 502–508.

(6) Rice, S. F.; Gray, H. B. *J. Am. Chem. Soc.* **1983**, *105*, 4571-4575.

(7) Che, C.-M.; Butler, L. G.; Gray, H. B.; Crooks, R. M.; Woodruff, W. H. *J. Am. Chem. Soc.* **1983**, *105*, 5492-5494.

(8) Stiegman, A. E.; Rice, S. F.; Gray, H. B.; Miskowski, V. M. *Inorg. Chem.* **1987**, *26*, 1112-1116.

(9) Fordyce, W. A.; Brummer, J. G.; Crosby, G. A. *J. Am. Chem. Soc.* **1981**, *103*, 7061-7064.

(10) Bryan, S. A.; Schmehl, R. H.; Roundhill, D. M. *J. Am. Chem. Soc.* **1986**, *108*, 5408–5412.

(11) Che, C.-M.; Atherton, S. J.; Butler, L. G.; Gray, H. B. *J. Am. Chem. Soc.* **1984**, *106*, 5143–5145.

(12) Vogler, A.; Kunkely, H. *Angew. Chem. Int. Ed. Engl.* **1984**, *23*, 316-317.

(13) Kim, J.; Fan, F. F.; Bard, A. J.; Che, C.-M.; Gray, H. B. *Chem. Phys. Lett.* **1985**, *121*, 543-546.

(14) Braterman, P. S.; Song, J.-I.; Vogler, C.; Kaim, W. *Inorg. Chem.* **1992**, *31*, 222-224.

(15) Hirani, B.; Li, J.; Djurovich, P. I.; Yousufuddin, M.; Oxgaard, J.; Persson, P.; Wilson, S. R.; Bau, R.; Goddard III, W. A.; Thompson, M. E. *Inorg. Chem.* **2007**, *46*, 3865-3875.

(16) Matsunami, J.; Urata, H.; Matsumoto, K. *Inorg. Chem.* **1995**, *34*, 202-208.

(17) Arrizabalaga, P.; Castan, P.; Geoffroy, M.; Laurent, J.-P. *Inorg. Chem.* **1985**, *24*, 3656-3660.

(18) Schmauke, T.; Einar Möller, E.; Roduner, E. *Chem. Commun.* **1998**, 2589–2590.

(19) Reaction of Pt(pop) with two equivalents of Cr^{2+} in aqueous solution produced a stable species that was tentatively assigned as $Pt(pop)^{6-}$.[39] However, this assignment cannot be correct, since the Cr^{3+}/Cr^{2+} potential (ca. -1.1 V) is more positive than the estimated $E(Pt(pop)^{4-/5-})$ value of -1.8 V. Moreover, the Raman spectrum of the product has a ν(Pt-Pt) band at lower wavenumber than in the Pt(pop) parent.[39]

(20) Heuer, W. B.; Totten, M. D.; Rodman, G. S.; Hebert, E. J.; Tracy, H. J.; Nagle, J. K. *J. Am. Chem. Soc.* **1984**, *106*, 1163-1164.

(21) Lam, Y. C., PhD Dissertation, California Institute of Technology, 2015.

(22) Vlček, A., Jr.; Gray, H. B. *J. Am. Chem. Soc.* **1987**, *109*, 286-287.

(23) Vlček, A., Jr.; Gray, H. B. *Inorg. Chem.* **1987**, *26*, 1997-2001.

(24) Smith, D. C.; Gray, H. B. In *ACS Symposium Series 394. The Challenge of d and f Electrons.*; Salahub, D. R., Zerner, M. C., Eds.; American Chemical Society: Washington, DC, 1989, pp 356-365.

(25) Bridgeman, A. J.; Cavigliasso, G.; Ireland, L. R.; Rothery, J. *J. Chem. Soc., Dalton Trans.* **2001**, 2095–2108.

(26) Hill, M. G.; Sykes, A. G.; Mann, K. R. *Inorg. Chem.* **1993**, *32*, 783–784.

(27) Hunter, B. M.; Villahermosa, R. M.; Exstrom, C. L.; Hill, M. G.; Mann, K. R.; Gray, H. B. *Inorg. Chem.* **2012**, *51*, 6898−6905.

(28) Frisch, M. J.; Trucks, G. W.; Schlegel, H. B.; Scuseria, G. E.; Robb, M. A.; Cheeseman, J. R.; Scalmani, G.; Barone, V.; Mennucci, B.; Petersson, G. A.; Nakatsuji, H.; Caricato, M.; Li, X.; Hratchian, H. P.; Izmaylov, A. F.; Bloino, J.; Zheng, G.; Sonnenberg, J. L.; Hada, M.; Ehara, M.; Toyota, K.; Fukuda, R.; Hasegawa, J.; Ishida, M.; Nakajima, T.; Honda, Y.; Kitao, O.; Nakai, H.; Vreven, T.; Montgomery, J. A., Jr.; Peralta, J. E.; Ogliaro, F.; Bearpark, M.; Heyd, J. J.; Brothers, E.; Kudin, K. N.; Staroverov, V. N.; Kobayashi, R.; Normand, J.; Raghavachari, K.; Rendell, A.; Burant, J. C.; Iyengar, S. S.; Tomasi, J.; Cossi, M.; Rega, N.; Millam, J. M.; Klene, M.; Knox, J. E.; Cross, J. B.; Bakken, V.; Adamo, C.; Jaramillo, J.; Gomperts, R.; Stratmann, R. E.; Yazyev, O.; Austin, A. J.; Cammi, R.; Pomelli, C.; Ochterski, J. W.; Martin, R. L.; Morokuma, K.; Zakrzewski, V. G.; Voth, G. A.; Salvador, P.; Dannenberg, J. J.; Dapprich, S.; Daniels, A. D.; Farkas, O.; Foresman, J. B.; Ortiz, J. V.; Cioslowski, J.; Fox, D. J.; Gaussian 09, Revision C.01, Gaussian, Inc.: Wallingford CT, 2009.

(29) *ADF2014.06, SCM, Theoretical Chemistry, Vrije Universiteit, Amsterdam, The Netherlands, http://www.scm.com*.

(30) Perdew, J. P.; Burke, K.; Ernzerhof, M. *Phys. Rev. Lett.* **1996**, *77*, 3865-3868.

(31) Adamo, C.; Scuseria, G. E.; Barone, V. *J. Chem. Phys.* **1999**, *111*, 2889-2899.

(32) Raghavachari, K.; Binkley, J. S.; Seeger, R.; Pople, J. A. *J. Chem. Phys.* **1980**, *72*, 650-654.

(33) Andrae, D.; Häussermann, U.; Dolg, M.; Stoll, H.; Preuss, H. *Theor. Chim. Acta* **1990**, *77*, 123-141.

(34) Martin, J. M. L.; Sundermann, A. *J. Chem. Phys.* **2001**, *114*, 3408.

(35) Glendening, E. D.; Badenhoop, J. K.; Reed, A. E.; Carpenter, J. E.; Bohmann, J. A.; Morales, C. M.; Landis, C. R.; Weinhold, F. Theoretical Chemistry Institute, University of Wisconsin, Madison, USA, 2013.

(36) Cossi, M.; Rega, N.; Scalmani, G.; Barone, V. *J. Comput. Chem.* **2003**, *24*, 669-681.

(37) Klamt, A.; Schüürmann, G. *J. Chem. Soc., Perkin Trans. 2* **1993**, 799 - 805.

(38) van Lenthe, E.; Ehlers, A.; Baerends, E. J. *J. Chem. Phys.* **1999**, *110*, 8943-8953.

(39) Alexander, K. A.; Paul Stein; Hedden, D. B.; Roundhill, D. M. *Polyhedron* 1983, 2, 1389-1392.